



Available online at www.sciencedirect.com
jmr&t
 Journal of Materials Research and Technology
 journal homepage: www.elsevier.com/locate/jmrt



Original Article

Strengthening mechanism of lamellar-structured Ti–Ta alloys prepared by powder metallurgy

Chufan Wang^a, Qi Cai^{a,*}, Jinxu Liu^{a,b,**}, Xifeng Yan^a

^a School of Materials Science and Engineering, Beijing Institute of Technology, Beijing, 100081, China

^b China National Key Laboratory of Science and Technology on Materials under Shock and Impact, Beijing Institute of Technology, Beijing, 100081, China

ARTICLE INFO

Article history:

Received 29 August 2022

Accepted 19 October 2022

Available online 22 October 2022

Keywords:

Ti–Ta alloys

Powder metallurgy

Lamellar microstructure

Mechanical properties

Strengthening mechanism

ABSTRACT

Titanium-tantalum alloys with lamellar microstructure were fabricated by cold isostatic pressing under 400 MPa and pressure-free sintering at 1600 °C. By such a low-cost powder metallurgy method, the Ti–Ta alloy exhibited the tensile yield strength of 1124 MPa at room temperature, which was twice that of the cast Ti–Ta alloys. The microstructure and mechanical properties were characterized in detail to elucidate the deformation behavior and the strengthening mechanism of the Ti–Ta alloys prepared by powder metallurgy. With the increasing Ta content, the width of the α laths decreased, and that of the β laths increased, leading to the precipitation of the acicular α in the β laths. Correspondingly, the yield and ultimate strength increased, while the strain to failure decreased. Lamellar structure strengthening was determined to be the dominating mechanism for the high strength of the Ti–Ta alloys prepared by powder metallurgy. After quantitatively evaluating the contributions of laths, solute atoms, prior β grain boundaries, and dislocations, a model was established to illustrate the yield strength of the Ti–Ta alloys. The calculated values agreed well with the measured strength values of the Ti–Ta alloys, indicating that this model is effective in forecasting the strength of the dual-phase Ti alloys with lamellar structure.

© 2022 The Authors. Published by Elsevier B.V. This is an open access article under the CC BY-NC-ND license (<http://creativecommons.org/licenses/by-nc-nd/4.0/>).

1. Introduction

The ideal biomedical materials for orthopedic implants are expected to possess outstanding biocompatibility, good corrosion resistance, high strength, certain plasticity, and low elastic modulus [1,2]. In comparison to traditional metallic biomaterials such as stainless steel and Co–Cr alloys,

titanium and its alloys are regarded as the most suitable candidate for hard tissue implants due to their higher specific strength, superior biocompatibility, and better corrosion resistance [3,4]. Commercially pure titanium (CP–Ti) was the first generation of biomedical material for half a century. Afterward, since the low-strength CP–Ti was unable to meet the requirement of some hard tissues [5,6], the Ti–6Al–4V (TC4)

* Corresponding author.

** Corresponding author.

E-mail addresses: caiqi6406608@163.com (Q. Cai), liujinxu@bit.edu.cn (J. Liu).

<https://doi.org/10.1016/j.jmrt.2022.10.095>

2238-7854/© 2022 The Authors. Published by Elsevier B.V. This is an open access article under the CC BY-NC-ND license (<http://creativecommons.org/licenses/by-nc-nd/4.0/>).

alloy with high strength became the most widely employed biomedical alloy, taking up 50% of the Ti products [7]. However, the release of Al and V ions might result in long-term health problems, such as neurological diseases [8] and Alzheimer's diseases [9]. Therefore, the development of new titanium alloys with high strength without harmful Al and V elements is of great importance in the biomedical field. Many efforts were devoted to the β -type titanium alloys consisting of non-toxic elements [10]. Yilmaz et al. fabricated a series of Ti–Nb based alloys as potential implant materials, including porous Ti–Nb alloys, Ti–Nb–Zr alloys, Ti–Nb–Sn alloys, and porous Ti–Nb–Zr–Ta alloys [11–14]. The elastic modulus of the alloys was as low as 35–15 GPa, which meet the requirements of orthopedic implants. Studies were also implemented on binary Ti–Ta alloys. Due to the solid-solution strengthening effect of the Ta element and the stable Ta₂O₅ passive films, the Ti–Ta alloy had high strength [15] and good corrosion resistance [16]. Huang et al. [17] reported the Ta addition led to the phase transformation of $\alpha \rightarrow \alpha' \rightarrow \alpha'' + \alpha' \rightarrow \beta + \alpha'' + \alpha'$. With the increasing Ta content, the yield strength of the Ti–Ta alloys increased first and then decreased, and the peak strength occurred at the composition of Ti-30 wt%Ta. An inverse trend was found for the Young's modulus. Such variation tendency of the strength was common in the Ti–Ta alloys with different Ta contents [18]. Zhou et al. investigated the microstructure and the mechanical property of the Ti-50 wt%Ta alloys after heat treatment [19]. The alloy after homogenization exhibited the α'' structure, which was sensitive to the aging temperature and duration. By aging at 564 °C for 72 h, the obtained $\alpha + \beta$ structure led to better combined mechanical properties, i.e. low modulus, high strength, and moderate plasticity.

The above research mainly focused on the as-cast Ti–Ta alloys. Nonetheless, titanium and tantalum have different melting points (Ti, 1668 °C, and Ta, 2996 °C) and density (Ti, 4.51 g·cm⁻³, and Ta, 16.60 g·cm⁻³) [20], which would lead to the composition segregation during the solidification [21]. To avoid this drawback, Ti–Ta alloys had to be remelted more than ten times to ensure homogeneity [22]. Such a complicated manufacturing process hindered the broad application of the Ti–Ta alloys.

Powder metallurgy (PM), the method of fabricating strong and ductile Ti–6Al–4V alloy in the previous research, was applied with many advantages over the traditional casting methods [23]. Preparing Ti–Ta alloys by powder metallurgy would be a feasible approach to improve the performance. Liu et al. [24] fabricated a series of Ti–Ta alloys of a dual structure consisting of Ti-rich and Ta-rich zones by cold isostatic pressing and vacuum sintering. The Ti–Ta alloys prepared by powder metallurgy showed higher tensile strength and lower elastic modulus than the ingot metallurgical alloys. Xu et al. [15] prepared a lamellar-structured Ti–Ta alloy by powder metallurgy and hot swagging. Due to the precipitation strengthening of the fine α phase inside Ti-enriched zones and fine β grains in the Ta-enriched zones, the Ti–Ta alloy showed an ultra-high tensile strength (σ_{UTS}) of 1570 MPa. Besides improving the mechanical properties of alloys, powder metallurgy is a cost-efficient technique for fabricating high-quality products with complex geometries such as surgical implants [25] due to the characteristic of near-net-shape

forming. Therefore, powder metallurgy promotes the manufacturing of biomedical Ti–Ta alloys with excellent mechanical properties at a low cost.

Understanding the relationship between the microstructure and the mechanical properties is crucial to developing high-performance alloys. Generally, the morphology and the size of the α phase significantly affect the mechanical properties [26]. The micro-sized α precipitates in lamellar structure or Widmanstätten structure of titanium alloys are ductile, and the dislocation slipping preferentially starts at the softer α [27]. Semiatin et al. conducted hot compression tests on Ti–6Al–4V alloys containing α laths, and they found that the peak stress had a significant Hall–Petch dependence on the thickness of the α platelet at lower temperatures [28]. Wen et al. further pointed out that the tensile strength increased with the refinement of the α colony and plates [29]. In addition, the nanoscale acicular α might precipitate in the β matrix, which was regarded as a hard-to-deform phase [30] and significantly contributed to the strength. Mantri et al. [31] tuned the scale of the α precipitates through tailoring heat treatment parameters, and they found that the ultimate tensile strength increased with an increasing number density of α precipitates. Chong et al. [32] claimed that the acicular α strengthened the β matrix, and the dislocations piled up at the interfaces of the α and the transformed β regions (β with acicular α precipitates), which provided additional reinforcements for the alloy. Liang et al. [33] proposed a quantitative relationship between microstructure and strength, indicating the strengthening mechanism of the Ti–30Zr–5Al–3V (wt.%) alloys. However, only two features of the microstructure, the thickness of the α laths and the volume fraction of the β phase, were taken into consideration. Similarly, Tan et al. [27] established a formula to predict the strength of the Ti alloy by introducing the parameters of the volume fraction and the width of the α and β laths, whereas the effects of the grain boundary and the solid solution element were not included. Therefore, to systematically understand the relationship between the microstructure and the strength of the Ti alloy, a quantitative calculation formula should be developed by incorporating multiple influencing factors about the microstructure.

Overall, the previous studies focused on the fabrication of multi-element Ti alloys rather than “simplified” ones, and the Ti alloys containing refractory metal elements were commonly fabricated by complicated melting, hot deformation, and posttreatment. In this study, the authors aim to reduce the production cost of shaped Ti-alloy components by using a cost-effective powder metallurgy method. Binary Ti–Ta alloys were prepared as potential implant materials. The relationship among the composition, microstructure, and strength was investigated, and the deformation behavior of the Ti–Ta alloys was discussed. In addition to the qualitative analysis, the contributions of lamellar structure strengthening, solid solution strengthening, grain boundary strengthening, and dislocation strengthening to the yield strength were quantitatively calculated. A strength prediction model of the two-phase titanium alloys with lamellar microstructure similar to the Ti–Ta alloys was then developed. This model provides a theoretical basis for the subsequent composition design, microstructure regulation, mechanical properties prediction and analysis of multi-element titanium alloys.

2. Experimental details

The Ti- x Ta ($x = 15, 20$, and 25 , wt.%) alloys (referred as Ti-15Ta, Ti-20Ta and Ti-25Ta hereafter) were prepared from elemental powders of Ti (purity >99.9%, particle size <45 μm) and Ta (purity >99.9%, particle size <10 μm). The powders were ball-milled by a planetary ball mill at a speed of 200 rpm for 2 h, and the weight ratio of balls to powders was 15:1. Then, the homogeneously mixed powders were compacted in a cylindrical mold using a cold isostatic press under 400 MPa for 80 min. Afterward, the green compacts were sintered at 1600 $^{\circ}\text{C}$ for 3 h in an argon atmosphere. The heating and cooling rate were both 3.5 $^{\circ}\text{C}/\text{min}$, and the argon gas flow was 1 L/min.

Quasi-static tensile and compression tests were conducted on an Instron 5985 electronic universal testing machine with a strain rate of $1 \times 10^{-3} \text{ s}^{-1}$. The gauge section of tensile specimens was $\Phi 5 \times 30 \text{ mm}$ with an extensometer, the dimensions of the cylindrical compression specimens are $\Phi 5 \times 5 \text{ mm}$. Phase identification was performed by an MXP21-VAHF X-ray diffraction (XRD) analyzer with Cu K α radiation ($\lambda = 0.15406 \text{ nm}$) on bulk samples of $\Phi 10 \times 10 \text{ mm}$. Scanning electron microscopy (SEM) analyses were performed in a ZEISS-Gemini300 microscope equipped with an energy-dispersive X-ray spectroscopy (EDS) analyzer to determine the chemical composition of the selected area. The specimens were mechanically ground with increasing grades of SiC abrasive papers and then polished with Fe $_2$ O $_3$ -H $_2$ O solution and Cr $_2$ O $_3$ -H $_2$ O solution in sequence. Statistical analyses of microstructure parameters on SEM images were conducted by Image-Pro Plus software. Transmission electron microscopy (TEM) analyses were conducted using a JEOL-2100f microscope under an accelerating voltage of 300 kV. Thin foils for TEM were firstly cut at $\Phi 5 \times 0.5 \text{ mm}$ and polished to a thickness of 100 μm with abrasive papers. Then, the specimens were continuously thinned to 50 μm by twin-jet electro-polishing using a 4 vol% perchloric acid solution in methanol at -20°C . The deformed specimens were sectioned parallel to the compression axis, and the microstructural characterizations was performed on this specimen section.

3. Results

3.1. Phase constitution and microstructure of Ti-Ta alloys by powder metallurgy

Fig. 1 shows the XRD profiles obtained from the as-sintered Ti- x Ta alloys, and the characteristic peaks of the α and β phases are indicated. The three Ti-Ta alloys were comprised of body-centered cubic (bcc) β phase and hexagonal closed-packed (hcp) α phase. Using the Rietveld refinement method, the volume fraction of the two phases was calculated and summarized in Table 1. Overall, the Ti-(15–25)Ta alloys were α -phase-dominated, and the volume fraction of the α phase was larger than 80.0 vol%. The Ti-15Ta contained the lowest proportion of the β phase (7.1 vol%) and the highest proportion of the α phase (92.9 vol%). When 5 wt% more Ta was added, the volume fraction of the β phase was increased to 11.4%, and the

volume fraction of the α phase was decreased to 88.6%. When the Ta content reached 25 wt%, the content of the β phase was further increased to 16.2 vol%, and that of the α phase was decreased to 83.8 vol%. The increase of Ta content brought about more β phase and less α phase to the Ti-Ta alloys. This was ascribed to the β -phase stability of the Ta element, which improved the resistance for the $\beta \rightarrow \alpha$ transition upon cooling. Thus, the increasing Ta content would lead to the increasing content of the β phase that was stabilized to room temperature [34].

Fig. 2 shows the microstructure of the as-sintered Ti-Ta alloys. The alloys presented lamellar structure, which consisted of continuous grain-boundary (GB) α decorated on the prior β grain boundary, and lamellar α embedded inside the prior β grains. To illustrate the differences among the microstructures of the Ti-Ta alloys, the size of the prior β grains was measured by the Image-Pro Plus software, as well as the thicknesses of the grain-boundary α , and that of the lamellar α , as summarized in Table 1. The prior β equiaxed grains were clearly distinguished in Fig. 2(a), (d), and (g), as enclosed by dark continuous GB α . The average grain size slightly decreased with the increase of Ta content, e.g. 84.8 μm for Ti-15Ta and 75.2 μm for Ti-25Ta, which indicated that the solution of Ta could refine the β grains. This could be explained by the slower diffusion rate of Ta than Ti in the β -Ti [35], which could hinder the migration of grain boundaries during high-temperature sintering. Fig. 2(b), (e), and (h) shows the specific microstructure morphology at higher magnifications. The GB α and lamellar α became thinner with the increasing Ta content. Meanwhile, the bright β laths separated by the lamellar α became thicker, which was consistent with the rules of the phase constitution obtained from the XRD patterns. In addition, acicular α phases precipitated in wider β laths (marked as the β_{trans} domain) in the Ti-20Ta and Ti-25Ta alloys, and the density and size of the acicular α in the Ti-25Ta alloy were larger than those in the Ti-20Ta alloy (Fig. 2(c), (f), and (i)). This phenomenon was related to the nucleation and growth mechanism of the acicular α [26]. It was reported that some precipitate-free zones would remain inside the grains at the end of the cooling stage, and the α could precipitate in acicular morphology in these zones. With the increasing Ta content, more β phases were remained as precipitate free zones upon cooling, promoting the nucleation and the growth of more acicular α phases.

3.2. Mechanical properties of Ti-Ta alloys by powder metallurgy

Fig. 3 shows the quasi-static tensile and compressive curves of the Ti-Ta alloys at room temperature. The corresponding ultimate strength, yield strength, and critical fracture strain are listed in Table 2. In the tensile test, the yield strength of the Ti-15Ta alloy was 942 MPa with an elongation of 2.4%. The Ti-20Ta alloy exhibited a higher yield strength of 1086 MPa and lower ductility of 1.4%. The Ti-25Ta alloy showed the highest yield strength of 1124 MPa but the lowest ductility of 1.1%. In terms of compressive properties, as more Ta elements were added in the Ti-Ta alloys, the yield strength increased but the critical fracture strain decreased, which had the same change rule as the tensile property. The tensile properties of

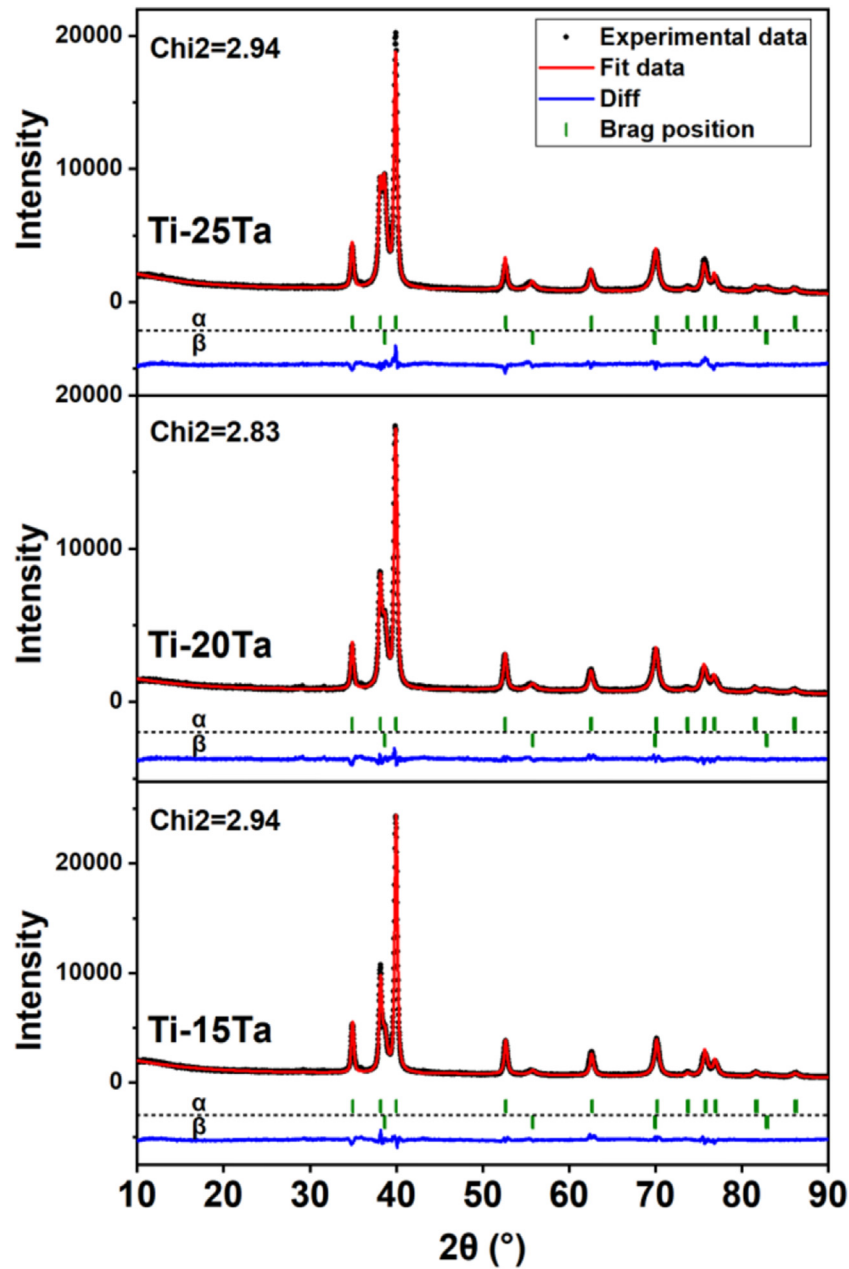


Fig. 1 – XRD patterns of the sintered Ti-xTa alloys by powder metallurgy.

the Ti-Ta alloys fabricated by powder metallurgy, cast, and selective laser melting (SLM) are shown in Fig. 4. The strength of the Ti-Ta alloys prepared by powder metallurgy in this paper is twice larger than that of traditional cast Ti-Ta alloys.

Therefore, the Ti-Ta alloys by low-cost powder metallurgy are the promising materials as implants in the medical application, where the requirements were mostly on high strength, rather than high plasticity.

Table 1 – Phase constituents and microstructure parameters of Ti-xTa alloys.

Alloys	Volume fraction (%)		Width (μm)			Grain size (μm)
	α	β	GB α	lamellar α	acicular α	
Ti-15Ta	92.9	7.1	9.6 ± 1.6	3.6 ± 1.4	/	84.9 ± 22.0
Ti-20Ta	88.6	11.4	7.4 ± 1.6	2.8 ± 1.4	0.197	81.4 ± 29.1
Ti-25Ta	83.8	16.2	4.3 ± 0.6	2.0 ± 0.9	0.287	75.2 ± 35.2

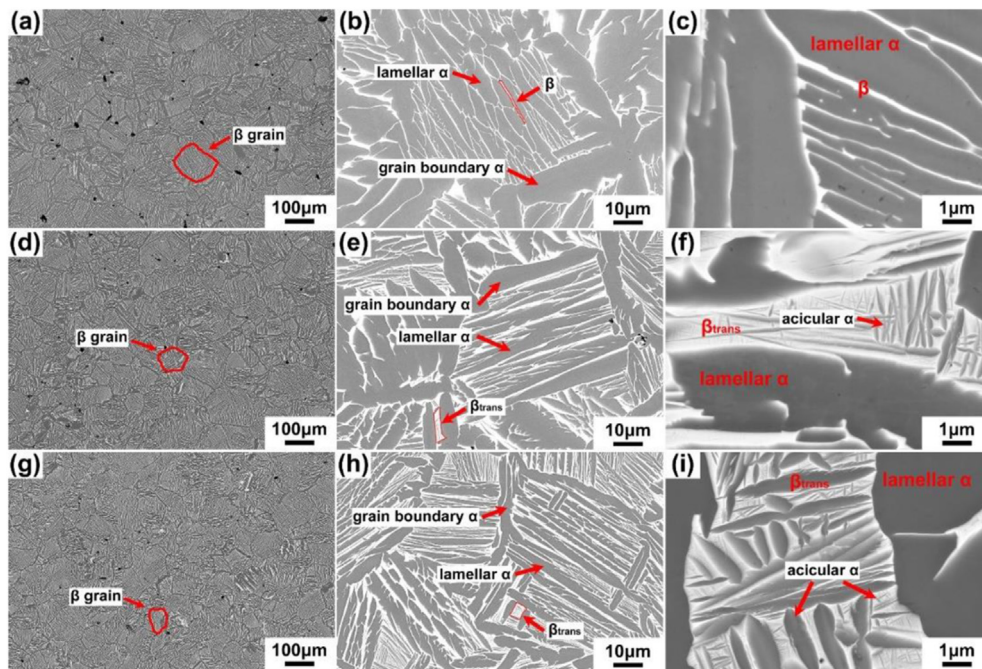


Fig. 2 – Backscattered electron (BSE) images of (a–c) Ti–15Ta alloy, (d–f) Ti–20Ta alloy, and (g–i) Ti–25Ta alloy. Magnifications (a), (d), and (g) $100\times$, (b), (e), and (h) $1000\times$, and (c), (f), and (i) $10,000\times$. The regions with dark and bright contrasts correspond to the α and β regions, respectively.

4. Discussion

4.1. Deformation behavior of Ti–Ta alloys by powder metallurgy

The design and development of metallic materials with high strength as orthopedic implants is the pursuit of the biomedical material field [40]. The second-phase strengthening is one of the most effective methods to develop ultra-high-strength alloys. However, the plate-like α phase in the powder metallurgical Ti–Ta alloys is 2–4 μm in size, which is beyond the size range of the second phase for dispersion strengthening. To date, the effect of the thick α laths on the mechanical properties of Ti alloys is still not clear. In addition, since the strength, volume fraction, and crystal structure of the lamellar α and β phases are all different [41], they play different roles during plastic deformation. Therefore,

understanding the deformation behavior of the α and β phases in the lamellar microstructure is of great significance for unveiling the relationship between the microstructure and mechanical properties of the powder metallurgical Ti–Ta alloys.

The deformed microstructures near the fracture area of the Ti–15Ta and Ti–25Ta alloys are shown in Fig. 5. The β laths in the Ti–15Ta alloy are interrupted into parallel segments after deformation, as shown in Fig. 5(a). The formation of the steps is due to the slip transmission through the α and β laths [27,42,43]. The slip lines sheared through the whole β lath, suggesting that the α/β interfaces provided little resistance to slip transmission, and the dislocations had relatively long effective slip length. Such penetration of slipping through the α and β laths could account for the moderate strength and high plasticity for the Ti–15Ta out of the three alloys. Fig. 5(b) shows the deformation characteristics of the Ti–25Ta alloy. Within the same shear band, the thin β laths were interrupted

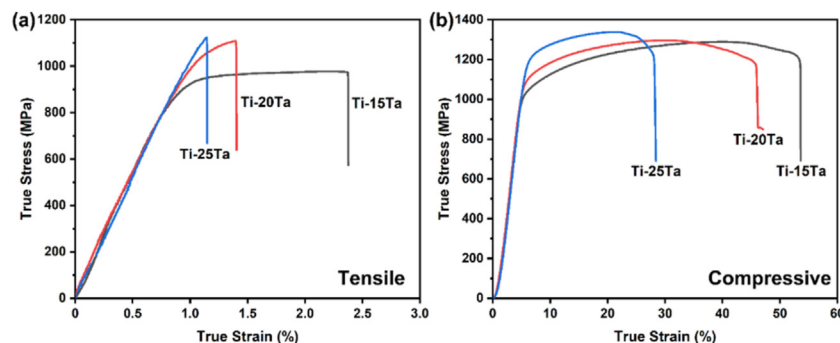


Fig. 3 – True (a) tensile and (b) compressive stress-strain curves of Ti–Ta alloys by powder metallurgy.

Table 2 – Tensile and compressive properties of Ti–Ta alloys by powder metallurgy.

Alloys	Tensile yield strength (MPa)	Ultimate tensile strength (MPa)	Elongation (%)	Compressive yield strength (MPa)	Ultimate compressive strength (MPa)	Critical fracture strain (%)
Ti–15Ta	942	977	2.4%	968	1288	52%
Ti–20Ta	1086	1107	1.4%	1034	1299	45%
Ti–25Ta	1124	1124	1.1%	1106	1340	27%

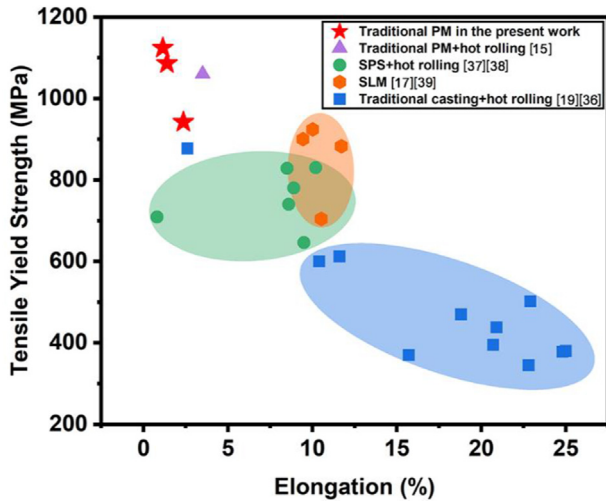


Fig. 4 – Tensile yield strength and elongation of Ti–Ta alloys prepared by casting, powder metallurgy, and selective laser melting [15,17,19,36–39]. The results in the present work are indicated by red stars.

into pieces, whereas the thick β_{trans} domains containing acicular α phases were hardly cut off. This indicated that the acicular α phases strengthened the β matrix, which improved the resistance of the interfaces. Therefore, the dislocations were unable to transmit the β_{trans} domains, shortening the effective slip length [44]. Since the Ti–25Ta alloy contained much more β_{trans} phase, this alloy exhibited the highest strength and lowest plasticity out of the three alloys.

The TEM observations were performed on the α/β interface in the Ti–15Ta alloy before and after deformation to elucidate the slip transmissions. Fig. 6(a) shows the bright-field TEM image of the Ti–15Ta alloy before deformation. The dark and

bright areas were β and α phases, respectively. The selected area electron diffraction (SAED) pattern shows that the α lath and the β matrix obeyed the classic Burgers orientation relationship (BOR) of $(\bar{1} 10)\beta // (0001)\alpha$ and $[111]\beta // [2 \bar{1} 1 0]\alpha$ [45]. Furthermore, the high-resolution lattice-scale TEM image and the enlarged figures for the arrangement of the atoms of the α and β phases are presented in Fig. 6(b). At the two sides of the interface, the crystalline interplanar spacing of $(0002)\alpha$ and $(110)\beta$ are 0.235 nm and 0.233 nm, respectively, forming a semi-coherent phase boundary. Fig. 6(c) shows the slip step due to the slip transmission of the semi-coherent α/β interface. The slip system in the β lath is $\langle 111 \rangle (110)$, which is identified by the SAED pattern. Based on the BOR between the α and β phases, it was demonstrated that the dislocations were firstly activated at $\{0001\} \langle 11 \bar{2} 0 \rangle$ in the soft α laths, and then continued to slip at $\{110\} \langle 111 \rangle$ in the adjacent β lath. Finally, slip steps were formed when the dislocation passed through the entire β lath. As shown in Fig. 6(c), the entangled dislocations only existed at the left side of the β lath. In addition, since the lamellar α phases in the same colony had the same crystal orientation, the dislocations could continuously pass through several adjacent α phases at the same slip systems. Thus, multiple slip steps appeared in a shear band (Fig. 5(a)). In general, parallel slip systems between the adjacent α and β phases facilitated the dislocations passing through the semi-coherent phase boundaries.

Fig. 7 shows the TEM images of the Ti–25Ta alloy after deformation. The acicular α precipitated in the β lath, and the strengthened β lath became curly during the deformation, rather than be cut off (Fig. 7(a)). Differed from the location of the dislocations in Fig. 6(c), the dislocations in the α phase piled up at both sides of the β lath, especially at the interface, suggesting that the $\alpha/\beta_{\text{trans}}$ interface provided large resistance to shearing. The high-resolution lattice-scale image of the α and β phases on either side of the $\alpha/\beta_{\text{trans}}$ interface is shown in Fig. 7(b), and the inverse fast Fourier transform (IFFT) images

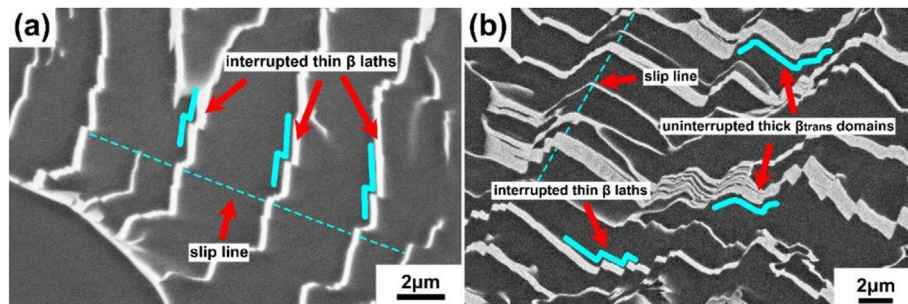


Fig. 5 – SEM images of (a) Ti–15Ta alloy, and (b) Ti–25Ta alloy after deformation.

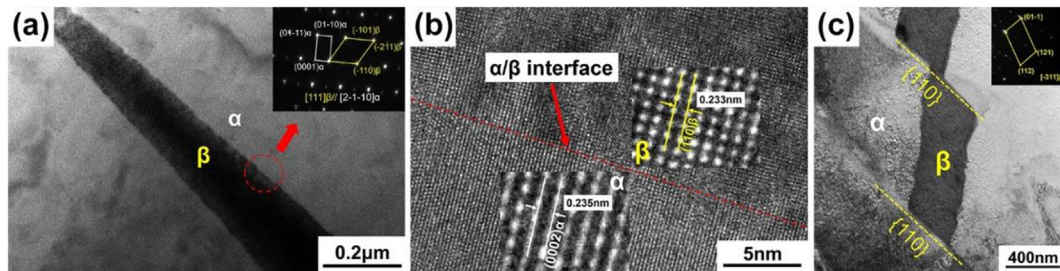


Fig. 6 – (a) Bright-field TEM image and corresponding SAED pattern of the undeformed Ti–15Ta alloy, (b) high-resolution lattice-scale image of the undeformed Ti–15Ta alloy, and (c) bright-field TEM image of the deformed Ti–15Ta alloy.

corresponding to the rectangles are shown in Fig. 7(c) and (f). One could observe the lattice distortion in the α and β phase, including a number of extra half planes. The two strain maps, corresponding to the region of Fig. 7(c) and (f), were obtained from two different reflections using the open-source plugin (Geometric Phase Analysis) by Humboldt-Universität zu Berlin. The area of the bright color corresponded well to the regions surrounded by the dislocations, indicating high strain. Under the deformation, the β lath containing acicular α played the role of a strong barrier to the dislocations. Therefore, the Ti–25Ta alloy possessed the highest strength and lowest plasticity among the three alloys. We made a comparison among the mechanical properties of the reported Ti–Ta alloys in Fig. 4. The high yield strength (1068 MPa) of the hot swaged Ti–Ta alloys was attribute to the strengthening of the fine α -phase precipitates and that of the fine grains (5–40 μm). For the selective laser melted Ti–Ta alloy, the nano-sized acicular α'' (52–79 nm) led to precipitation strengthening, and the yield strength was 920 MPa. However, the porosity and the unmelted Ta should be responsible for the decreased strength in the SLMed ally, compared with that of the hot swaged alloy. The melted Ti–Ta alloys exhibited equiaxed β and needle-like α'' structure, which provided precipitation strengthening, and

the yield strength was 400–610 MPa. After aging at 450–600 $^{\circ}\text{C}$, ω and α phases precipitated, and the yield strength was increased to 612–877 MPa. The Ti–Ta alloys by spark plasma sintering and hot forging showed the microstructure of equiaxed β and grain-boundary α . The increasing dislocation density by hot forging was the reason for the high strength of 868 MPa. Pure β -phase Ti–Ta alloy with the grain size of only $10.20 \pm 7.68 \mu\text{m}$ was prepared by the SLM method, and the high yield strength of 883 MPa might originate from the grain refinement strengthening. The Ti–Ta alloys by spark plasma sintering and cold rolling showed the lamellar structure, which confined the dislocations, and the yield strength was 740–830 MPa. By contrast, the yield strength of the Ti–Ta alloys by pressureless sintering was 942–1124 MPa in this study. The increase of the yield strength was due to the fine α laths and the fine acicular α in the β laths. The lamellar α phases introduced phase boundaries into powder metallurgical Ti–Ta alloys. The generated α/β interfaces hindered the slip of the dislocations, which affected the effective slip distance, as well as the mechanical properties of the alloys. However, the magnitude of the interface resistance to slipping was related to whether acicular α phases precipitated in the β matrix. On the one hand, the dislocations could slip from α to β laths

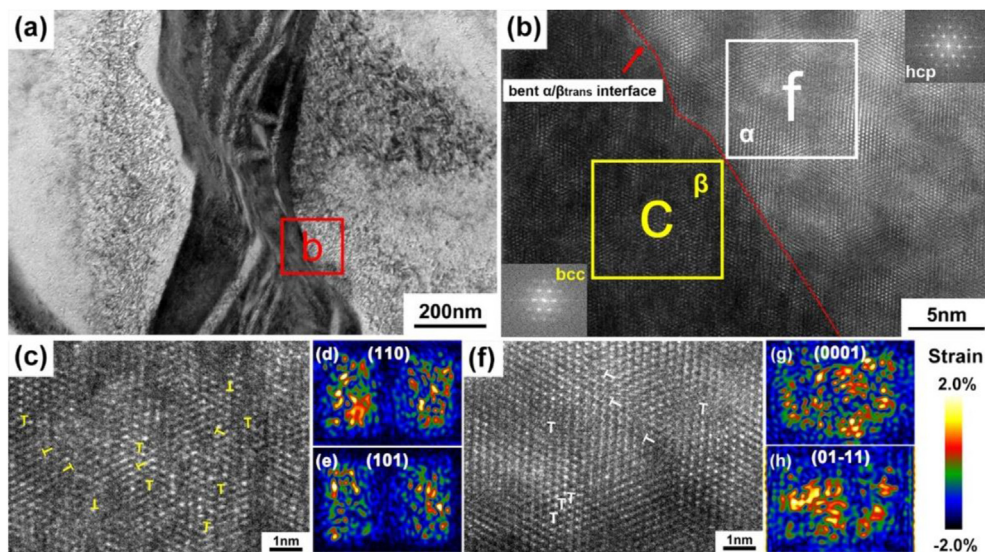


Fig. 7 – (a) TEM and (b) High-resolution lattice-scale image of the bent $\alpha/\beta_{\text{trans}}$ interface in the deformed Ti–25Ta alloy; (c) and (f) IFFT images corresponding to the rectangles in (b); (d) and (e) Strain maps corresponding to (c); (g) and (h) Strain maps corresponding to (f).

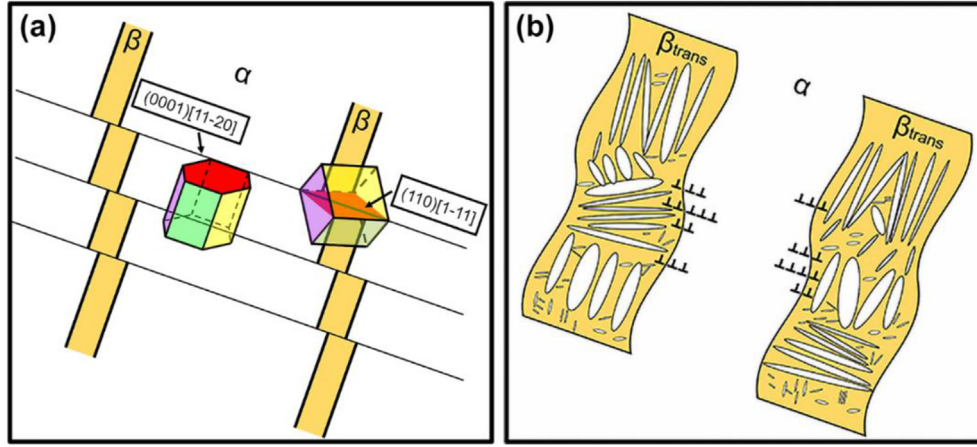


Fig. 8 – Schematic diagram of dislocations interaction with interfaces in powder metallurgical Ti–Ta alloys (a) without and (b) with acicular α phases in the β laths.

across the interface, when no acicular α generated in the β phase. On the other hand, the dislocations piled up at the $\alpha/\beta_{\text{trans}}$ interface when the acicular α precipitates strengthened the β laths. Therefore, the capability of the dislocations passing through the interface is the main concern for evaluating the mechanical properties of the Ti–Ta alloy by powder metallurgy. Fig. 8 shows the schematic diagram of two cases of the interaction between dislocations and interfaces in powder metallurgical Ti–Ta alloys.

4.2. Strengthening mechanism of Ti–Ta alloys by powder metallurgy

Previous studies demonstrated that the thickness of the α and β phases influenced the strength of the titanium alloys [28,29]. However, based on the discussion of the deformation behavior in the previous section, the dislocations interacted with the phase boundary during deformation, indicating that the interfaces also had an impact on the strength. Interactive stress could be induced to maintain the compatibility at the α/β interface. Therefore, it was necessary to consider the interactive stress when investigating the contribution of the lamellar α and β to the strength. Tan et al. [27] modified the rule of mixtures by introducing the interaction term to calculate the yield strength (Eqs. (1) and (2)).

$$\sigma_{\text{ls-1}} = \sigma_{\alpha} V_{\alpha} + \sigma_{\beta} V_{\beta} - m I_{\alpha\beta} \quad (1)$$

$$\sigma_{\text{ls-2}} = \sigma_{\alpha} V_{\alpha} + \sigma_{\beta\text{trans}} V_{\beta\text{trans}} - n I_{\alpha\beta\text{trans}} \quad (2)$$

Eq. (1) is suitable for calculating the strength of the Ti–15Ta alloy containing α and β laths, while Eq. (2) is suitable for calculating that of the Ti–20Ta and Ti–25Ta alloys since acicular α phases precipitated in most of the β laths. In the two equations, V_{α} is the volume fraction of the α phase, V_{β} is the volume fraction of the β phase, $V_{\beta\text{trans}}$ is the volume fraction of the β_{trans} domains, m is the coefficient of the interaction stress of the α/β interface, which is -4.65 , n is the coefficient of the interaction stress of the $\alpha/\beta_{\text{trans}}$ interface which is -0.58 , and $I_{\alpha\beta}$ and $I_{\alpha\beta\text{trans}}$ are respectively the barrier stress of the α/β

interface and the $\alpha/\beta_{\text{trans}}$ interface, which can be calculated by the following equations.

$$I_{\alpha\beta} = \tau_{\beta} - \tau_{\alpha} \quad (3)$$

$$I_{\alpha\beta\text{trans}} = \tau_{\beta} - \tau_{\alpha} + \Delta\tau \quad (4)$$

$$\tau = \frac{2G}{1-\nu} \exp\left(\frac{2\pi a}{b(1-\nu)}\right) \quad (5)$$

where τ_{α} and τ_{β} are the Peierls stress in α and β phase, which were calculated to be 37 MPa and 65 MPa, respectively, according to Eq. (5). In this equation, G is the shear modulus of β phase (48 GPa) and α phase (44 GPa), which were obtained by the calculation of the phase diagram (CALPHAD) method using the JMatPro 7.0 software, ν is the poison's ratio, 0.33, b is the Burgers vector of dislocations, 0.295 nm for the α phase [46] and 0.284 nm for the β phase [46], a is the lattice spacing of the slip plane, 0.257 nm for the (10 $\bar{1}$ 0) α and 0.233 nm for the (110) β . The results indicated that the dislocations must overcome 65.3 MPa in the α phase and 37 MPa in the β phase to initiate slipping. $\Delta\tau$ is the additional stress due to the strengthening of acicular α . Since the fine α is too hard to be deformed [46], the dislocations have to bow out and bypass these hard precipitates to slip further, consequently strengthening the matrix phase. Therefore, the contribution of the acicular α phase is considered as the second phase strengthening, and the increment of the strength can be calculated by the following Orowan equation [27].

$$\Delta\tau = \frac{Gb}{2\pi\lambda\sqrt{1-\nu}} \ln \frac{d}{r} \quad (6)$$

where G is the shear modulus of the β matrix, b is the Burgers vector of dislocations, λ is the interspace of the acicular α (Table 3), ν is the poison's ratio, 0.33, d is the diameter of precipitates (Table 3), which is approximately regarded as spherical, r is the core radius of dislocations, 0.284 nm $\Delta\tau$ was calculated as 228 MPa and 302 MPa for the Ti–20Ta and Ti–25Ta alloy, respectively. By incorporating the $\Delta\tau$ into Eq. (4), The $I_{\alpha\beta}$ for the Ti–15Ta alloy was 28 MPa, and the

Table 3 – Values of different symbols used in the strengthening mechanism calculations of the Ti-xTa alloys.

Symbol	Values			Unit
	Ti–15Ta	Ti–20Ta	Ti–25Ta	
X_i	13.7	15.1	15.9	at. %
ε	–0.163	–0.197	0.180	Dimensionless
d	/	149.0	232.9	Nm
λ	/	72.7	58.8	Nm
d_β	0.53	0.97	0.99	Mm

$I_{\alpha\beta\text{trans}}$ for the Ti–20Ta and Ti–25Ta alloys was 256 MPa and 330 MPa, respectively. For the lamellar α and β , the strength values of α (σ_α) and β (σ_β) in Eqs. (1) and (2) were estimated by applying the Hall-Petch relationship, as indicated by Eqs. (7) and (8), and the strength of the β_{trans} domains ($\sigma_{\beta\text{trans}}$) was estimated by Eq. (9).

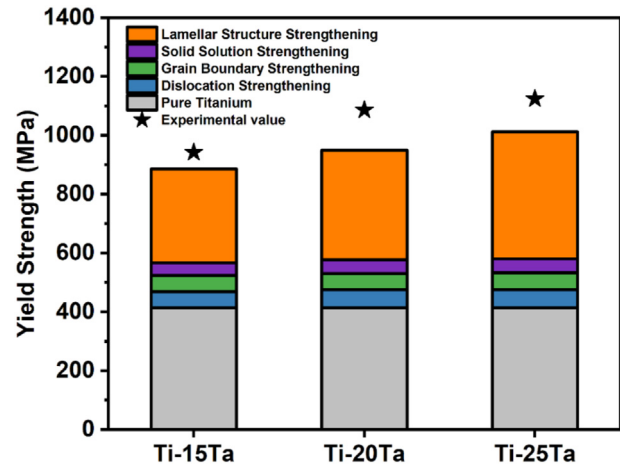
$$\sigma_\alpha = \sigma_{0\alpha} + k_\alpha d_\alpha^{-1/2} \quad (7)$$

$$\sigma_\beta = \sigma_{0\beta} + k_\beta d_\beta^{-1/2} \quad (8)$$

$$\sigma_{\beta\text{trans}} = \sigma_\beta + \Delta\tau \quad (9)$$

where $\sigma_{0\alpha}$ and $\sigma_{0\beta}$ are the friction stress for α and β , which are 182 MPa [47] and 802 MPa [48], respectively, the k_α and k_β are the Hall-Petch coefficients, which are $360 \text{ MPa} \cdot \mu\text{m}^{1/2}$ [47] and $500 \text{ MPa} \cdot \mu\text{m}^{1/2}$ [48], d_α and d_β are the average width of the α and β laths measured from the SEM images, as shown in Tables 1 and 3. The σ_α and σ_β for the Ti–15Ta alloy were 372 MPa and 1489 MPa, the σ_α was 396 MPa and 435 MPa for the Ti–20Ta and Ti–25Ta alloy, the $\sigma_{\beta\text{trans}}$ was 1538 MPa and 1607 MPa for the Ti–20Ta and Ti–25Ta alloy, respectively. The corresponding volume fraction (V_α , V_β , and $V_{\beta\text{trans}}$) was measured by the XRD profiles, and the values are shown in Table 1. Note that the volume fraction of the β laths without acicular α in the Ti–20Ta and Ti–25Ta alloys was to a limited content, which was ignored in this calculation. Therefore, the V_β values of the Ti–20Ta and Ti–25Ta alloy were approximately used as the $V_{\beta\text{trans}}$ values.

Based on Eqs. (1)–(9), the contributions to the yield strength from the lamellar structure were calculated to be 319 MPa, 373 MPa, and 431 MPa for the Ti–15Ta, Ti–20Ta, and Ti–25Ta alloys, respectively. Although the α and β laths were

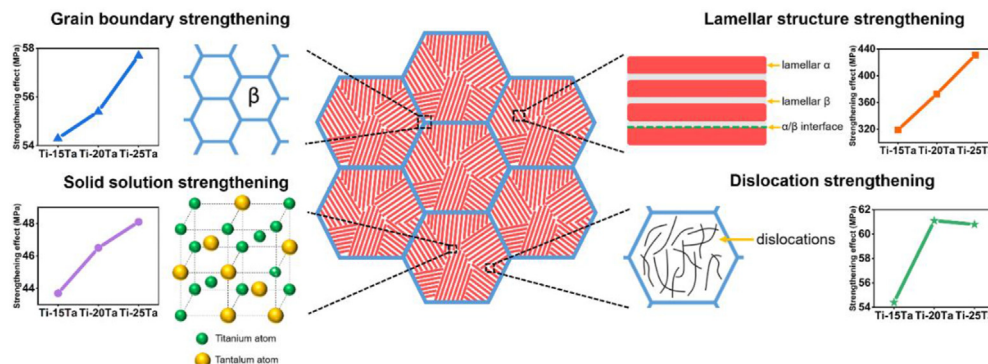
**Fig. 10 – Comparison of the calculated yield strength by the strength prediction model and the experimental tensile yield strength of powder metallurgical Ti-Ta alloys.**

the main characteristics of the powder metallurgical Ti-Ta alloys, other microstructure parameters also had an impact on the strength. Therefore, we further considered the contributions of the solid solution atoms, the prior β -phase grain boundary, and the dislocations to the strength of the Ti-Ta alloys. Note that the second phase strengthening of the acicular α phase has been considered in the strengthening effect of the lamellar structure.

Solid solution strengthening occurred when the Ta atoms were in the matrix as solutes. Due to the differences in size and shear modulus between the solute atoms and the solvent atoms, strain fields existed in the lattice. During the yielding process, the interaction between the dislocations and the strain fields would cause increases in the critical shear stress. The formulation was modified from the Fleischer model for substitutional solutes (Eq. (10)), expressing the normal stress generated by solid solution strengthening [49].

$$\sigma_{ss} = \left(\sum_i B_i^{3/2} X_i \right)^{2/3} \quad (10)$$

$$B_i = M \mu \lambda_i^{4/3} Z \quad (11)$$

**Fig. 9 – Schematic diagram of strengthening mechanisms of the powder metallurgical Ti-Ta alloys and the corresponding contribution values.**

where X_i is the atomic concentration of the solute i (Table 3), B_i is the strengthening coefficient for the solute i , which is $164 \text{ MPa} \cdot \text{at}^{-2/3}$ for the Ti–Ta binary system [49], M is the Taylor factor transforming shear stress to normal stress, which is 2.8 for β -Ti, μ is the shear modulus, Z is 0.9×10^3 , a factor associated with temperature [50], λ_i is a misfit parameter account for the lattice parameter misfit and the shear modulus misfit between Ti and solute atoms. The calculated values of solid solution strengthening are 44 MPa, 47 MPa, and 48 MPa for the Ti-15a, Ti-20Ta, and Ti-25Ta alloys, respectively.

The alloying Ta elements in titanium not only stabilized the β phase but also refined the prior β grains [15], which was also confirmed by the above results. Small grains have high-density grain boundaries, which would impede the dislocations moving to the neighboring grains [51]. The grain-boundary strengthening mechanism followed the Hall-Petch relationship [49].

$$\sigma_{gb} = kD^{-1/2} \quad (12)$$

where k is $500 \text{ MPa} \cdot \mu\text{m}^{1/2}$ for β -Ti [48], D is the average grain diameters measured from the SEM images, shown in Table 1. Thus, the strengthening effect caused by the refinement of the prior β grains was 54 MPa, 55 MPa, and 58 MPa for the Ti-15Ta, Ti-20Ta, and Ti-25Ta alloys, respectively.

Dislocations interacted with each other and impeded their motion by tangling. High dislocation density led to the reduction of the slip distance, enhancing the strength of the alloys. The contribution from the dislocations was described by the Taylor relationship [52].

$$\sigma_{dis} = M\alpha G b \rho^{1/2} \quad (13)$$

where M is the Taylor factor which is 2.8 for β -Ti, α is a constant equaling to 0.2, G is the shear modulus, 48 GPa, b is the Burgers vector, ρ is the dislocation density [53], as calculated by Eq. (13)).

$$\rho = \frac{3\sqrt{2}\pi(\epsilon^2)^{1/2}}{Db} \quad (14)$$

where D , and ϵ are the average grain size of prior β phases (shown in Table 1), and the microstrain inside, respectively. The microstrain ϵ were obtained from the XRD profiles (Table 3). The values from the dislocation strengthening were estimated to be 54 MPa, 61 MPa, and 61 MPa for the Ti-15a, Ti-20Ta, and Ti-25Ta alloys, respectively.

The strengthening mechanisms of the powder metallurgical Ti–Ta alloys were analyzed, and the schematic diagram is shown in Fig. 9. The contributions from the four categories of microstructure, i.e. the lamellar α and β laths, the solid solution atoms, the prior β grain boundaries, and the dislocations to the yield strength, were calculated. On this basis, a strength prediction model is developed by considering the four strengthening mechanisms.

here σ_{basis} is the basic strength of pure titanium, which is 414 MPa [54], σ_{ls} , σ_{ss} , σ_{gb} , and σ_{dis} are the contributions calculated from the four strengthening mechanisms, respectively. When the acicular α hardly precipitated in the β laths, the σ_y is described by Eq. (16).

$$\sigma_y = 1360 + \left(360d_{\alpha}^{-1/2} - 500d_{\beta}^{-1/2} - 620\right)V\alpha + 500d_{\beta}^{-1/2} + 1.2 \times 10^5 \left(\sum_i \lambda_i^2 X_i\right)^{2/3} + \frac{500 + 20.2(\epsilon^2)^{1/4}}{D^{1/2}} \quad (16)$$

According to Eqs. (15) and (16), the yield strength was calculated to be 885 MPa, 950 MPa, and 1012 MPa for the Ti-15Ta, Ti-20Ta, and Ti-25Ta alloy, respectively.

The comparison of the concluded strengthening contributions and the experimental value is shown in Fig. 10. The variation tendency of the predicted yield strength with the increasing Ta content agreed well with the measured value. Furthermore, the deviation between the predicted and the measured strength value was less than 150 MPa. Hence, the strength prediction model was proved to be valid, and the quantitative relationship between microstructure and strength in the two-phase Ti–Ta alloys with lamellar microstructure was successfully established.

5. Conclusions

In this study, high-strength Ti–Ta alloys with lamellar microstructure were fabricated by cold isostatic pressing and pressure-free sintering. The deformation behaviors and strengthening mechanisms of the Ti–Ta alloys were investigated in detail to interpret the relationship between the microstructure and mechanical properties. The main conclusions are summarized as follows.

- (1) The lamellar microstructure was formed in the Ti–Ta alloys prepared by powder metallurgy. With the increasing Ta content, the width and the volume fraction of the α laths decreased, while those of the β phase increased. The acicular α phase precipitated from the thick β laths in the Ti-20Ta and Ti-25Ta alloys.
- (2) The same variation trend was found in the compressive and tensile properties of the Ti–Ta alloys with the increasing Ta content, i.e. the yield and ultimate strength increased, while the strain to failure decreased. The Ti-25Ta alloy exhibited the highest tensile yield strength of 1124 MPa, which was twice that of casting Ti–Ta alloys.
- (3) Under plastic deformation, the dislocations interacted with the phase boundary of the α and β laths. When no acicular α phase precipitated in the β lath, dislocations

$$\sigma_y = \sigma_{basis} + \sigma_{ls} + \sigma_{ss} + \sigma_{gb} + \sigma_{dis} = 1360 + \left(360d_{\alpha}^{-1/2} - 500d_{\beta}^{-1/2} - 620\right)V\alpha + 500d_{\beta}^{-1/2} + \frac{2.6}{\lambda} \ln \frac{d_{aci}}{r} + 1.2 \times 10^5 \left(\sum_i \lambda_i^2 X_i\right)^{2/3} + \frac{500 + 20.2(\epsilon^2)^{1/4}}{D^{1/2}} \quad (15)$$

will transmit the α/β interface with a long effective slip distance. When the acicular α phases precipitated in the β lath, the $\alpha/\beta_{\text{trans}}$ interface will prevent dislocation from passing through the β lath, improving the strength of the alloy.

- (4) The lamellar structure strengthening is the dominating mechanism in the Ti–Ta alloys prepared by powder metallurgy. The contributions of lamellar structure strengthening, solid solution strengthening, grain boundary strengthening, and dislocation strengthening to the yield strength were quantitatively evaluated, and the proposed model was capable of predicting the strength of the Ti alloys with lamellar structure.

Data availability

The raw/processed data required to reproduce these findings cannot be shared at this time due to technical or time limitations.

Declaration of Competing Interest

The authors declare that they have no known competing financial interests or personal relationships that could have appeared to influence the work reported in this paper.

Acknowledgements

This work was supported by the National Natural Science Foundation of China [grant numbers 52171027], the Beijing Institute of Technology Research Fund Program for Young Scholars [grant number 202008002].

REFERENCES

- [1] Wang H, Luo HL, Chen JQ, Tang JC, Yao XY, Zhou YH, Yan M. Cost-affordable, biomedical Ti-5Fe alloy developed using elemental powders and laser in-situ alloying additive manufacturing. *Mater Charact* 2021;182:111526.
- [2] Wu J, Tan X, An X, Zhang J, Guo Y, Liu J, Luo Y, Yao W, Kong Q, Wang Q. Development of biomedical Ti-Nb-Zr-Mn alloys with enhanced mechanical properties and corrosion resistance. *Mater Today Commun* 2022;30:103027.
- [3] Liu YJ, Li XP, Zhang LC, Sercombe TB. Processing and properties of topologically optimised biomedical Ti-24Nb-4Zr-8Sn scaffolds manufactured by selective laser melting. *Mater Sci Eng A* 2015;642:268–78.
- [4] Tito Patricio MA, Lustosa CJR, Chaves JAM, Marques PWB, Silva PS, Almeida A, Vilar R, Florêncio O. Relationship between microstructure, phase transformation, and mechanical behavior in Ti-40Ta alloys for biomedical applications. *J Mater Res Technol* 2021;14:210–9.
- [5] Wang CS, Li CL, Zuo YT, Hong JK, Choi SW, Zhang GD, Mei Q, Park CH, Yeom JT. Tailoring bimodal structure for high strength and ductility in pure titanium manufactured via laser powder bed fusion. *J Alloys Compd* 2022;901:163590.
- [6] Chávez J, Jimenez O, Diaz-Luna J, Bravo-Barcenas D, Alvarado-Hernández F, Flores M, Suárez-Martínez R. Microstructure and corrosion characterization of a Ti-30Zr alloy with Ta additions processed by arc-melting for biomedical applications. *Mater Lett* 2021;284:129041.
- [7] Zhang L-C, Chen L-Y. A review on biomedical titanium alloys: recent progress and prospect. *Adv Eng Mater* 2019;21:1801215.
- [8] Nazari KA, Nouri A, Hilditch T. Mechanical properties and microstructure of powder metallurgy Ti-xNb-yMo alloys for implant materials. *Mater Des* 2015;88:1164–74.
- [9] Supriadi S, Lucky G, Sutowo C, Senopati G, Immanuel T, Suharno B. Developing beta titanium alloy Ti-6Mo-6Nb using vacuum arc furnace with manganese composition variation and variation of heat treatment duration for implant material applications, 5th International Symposium on Frontier of Applied Physics (ISFAP) part of Indonesian Science Expo. Indonesia: Tangerang Selatan; 2019.
- [10] Qi P, Li B, Wang T, Zhou L, Nie Z. Microstructure and properties of a novel ternary Ti-6Zr-xFe alloy for biomedical applications. *J Alloys Compd* 2021;854:157119.
- [11] Yilmaz E, Gökçe A, Findik F, Gulsoy HO, İyibilgin O. Mechanical properties and electrochemical behavior of porous Ti-Nb biomaterials. *J Mech Behav Biomed Mater* 2018;87:59–67.
- [12] Yilmaz E, Gökçe A, Findik F, Gulsoy HÖ. Assessment of Ti-16Nb-xZr alloys produced via PIM for implant applications. *J Therm Anal Calorim* 2018;134:7–14.
- [13] Yilmaz E, Gökçe A, Findik F, Gulsoy HÖ. Biomedical porous Ti-16Nb-10Zr-(0-15)Ta alloys. *Int J Mater Res* 2019;110:375–8.
- [14] Yilmaz E, Gökçe A, Findik F, Gulsoy HÖ. Powder metallurgy processing of Ti-Nb based biomedical alloys. *Acta Phys Pol A* 2018;134:278–80.
- [15] Xu S, Liu Y, Yang C, Zhao H, Lin B, Li J, Song M. Compositionally gradient Ti-Ta metal-metal composite with ultra-high strength. *Mater Sci Eng A* 2018;712:386–93.
- [16] de Souza KA, Robin A. Preparation and characterization of Ti-Ta alloys for application in corrosive media. *Mater Lett* 2003;57:3010–6.
- [17] Huang S, Sing SL, de Looze G, Wilson R, Yeong WY. Laser powder bed fusion of titanium-tantalum alloys: compositions and designs for biomedical applications. *J Mech Behav Biomed Mater* 2020;108:103775.
- [18] Zhou Y-L, Niinomi M, Akahori T, Nakai M, Fukui H. Comparison of various properties between titanium-tantalum alloy and pure titanium for biomedical applications. *Mater Trans* 2007;48:380–4.
- [19] Zhou Y-L, Niinomi M. Microstructures and mechanical properties of Ti-50 mass% Ta alloy for biomedical applications. *J Alloys Compd* 2008;466:535–42.
- [20] Dercz G, Matula I, Zubko M, Kazek-Kęsik A, Maszybrocka J, Simka W, Dercz J, Świec P, Jendzejewska I. Synthesis of porous Ti-50Ta alloy by powder metallurgy. *Mater Charact* 2018;142:124–36.
- [21] Zhang J, Rynko R, Frenzel J, Somsen C, Eggeler G. Ingot metallurgy and microstructural characterization of Ti-Ta alloys. *Int J Mater Res* 2014;105:156–67.
- [22] Zhou Y-L, Niinomi M. Ti-25Ta alloy with the best mechanical compatibility in Ti-Ta alloys for biomedical applications. *Mater Sci Eng C* 2009;29:1061–5.
- [23] Cao Y, Zeng F, Liu B, Liu Y, Lu J, Gan Z, Tang H. Characterization of fatigue properties of powder metallurgy titanium alloy. *Mater Sci Eng A* 2016;654:418–25.
- [24] Liu Y, Li K, Wu H, Song M, Wang W, Li N, Tang H. Synthesis of Ti-Ta alloys with dual structure by incomplete diffusion between elemental powders. *J Mech Behav Biomed Mater* 2015;51:302–12.
- [25] Ehtemam-Haghighi S, Attar H, Okulov IV, Dargusch MS, Kent D. Microstructural evolution and mechanical properties

- of bulk and porous low-cost Ti–Mo–Fe alloys produced by powder metallurgy. *J Alloys Compd* 2021;853:156768.
- [26] Sadeghpour S, Abbasi SM, Morakabati M, Bruschi S. Correlation between alpha phase morphology and tensile properties of a new beta titanium alloy. *Mater Des* 2017;121:24–35.
- [27] Tan C, Sun Q, Xiao L, Zhao Y, Sun J. Slip transmission behavior across alpha/beta interface and strength prediction with a modified rule of mixtures in TC21 titanium alloy. *J Alloys Compd* 2017;724:112–20.
- [28] Semiati SL, Bieler TR. The effect of alpha platelet thickness on plastic flow during hot working of Ti-6Al-4V with a transformed microstructure. *Acta Mater* 2001;49:3565–73.
- [29] Wen X, Wan M, Huang C, Lei M. Strength and fracture toughness of TC21 alloy with multi-level lamellar microstructure. *Mater Sci Eng A* 2019;740–741:121–9.
- [30] Wang S, Liang Y, Sun H, Feng X, Huang C. Tuning the number density of α s precipitates in Ti-6Al-2Sn-2Zr-3Mo-1Cr-2Nb-0.1Si alloys for achieving high strength. *J Alloys Compd* 2021;882:160732.
- [31] Mantri SA, Choudhuri D, Alam T, Viswanathan GB, Sosa JM, Fraser HL, Banerjee R. Tuning the scale of α precipitates in β -titanium alloys for achieving high strength. *Scr Mater* 2018;154:139–44.
- [32] Chong Y, Bhattacharjee T, Tsuji N. Bi-lamellar microstructure in Ti–6Al–4V: microstructure evolution and mechanical properties. *Mater Sci Eng A* 2019;762:138077.
- [33] Liang SX, Yin LX, Jiang RJ, Zhang XY, Ma MZ, Liu RP. Strengthening mechanism of two-phase titanium alloys with basketweave microstructure. *J Alloys Compd* 2014;603:42–7.
- [34] Kolli RP, Joost WJ, Ankem S. Phase stability and stress-induced transformations in beta titanium alloys. *JOM* 2015;67:1273–80.
- [35] Ansel D, Thibon I, Boliveau M, Debuigne J. Interdiffusion in the body cubic centered beta-phase of Ta-Ti alloys. *Acta Mater* 1998;46:423–30.
- [36] Zhou YL, Niinomi M, Akahori T. Effects of Ta content on Young's modulus and tensile properties of binary Ti–Ta alloys for biomedical applications. *Mater Sci Eng A* 2004;371:283–90.
- [37] Bahador A, Kariya S, Umeda J, Hamzah E, Kondoh K. Tailoring microstructure and properties of a superelastic Ti-Ta alloy by incorporating spark plasma sintering with thermomechanical processing. *J Mater Eng Perform* 2019;28:3012–20.
- [38] Huang Q, Xu S, Ouyang Z, Yang Y, Liu Y. Multi-scale nacre-inspired lamella-structured Ti-Ta composites with high strength and low modulus for load-bearing orthopedic and dental applications. *Mater Sci Eng C* 2021;118:111458.
- [39] Sing SL, Yeong WY, Wiria FE. Selective laser melting of titanium alloy with 50 wt% tantalum: microstructure and mechanical properties. *J Alloys Compd* 2016;660:461–70.
- [40] Kang L, Yang C. A review on high-strength titanium alloys: microstructure, strengthening, and properties. *Adv Eng Mater* 2019;21:1801359.
- [41] Banerjee D, Williams JC. Perspectives on titanium science and technology. *Acta Mater* 2013;61:844–79.
- [42] Liu X, Hao Y, Liu J, Li S, Cai Q, Lv Y. Comparison of high-temperature deformation behaviors for Ti-Al-Nb-V alloy with different initial microstructures at the strain of 0.7. *Mater Sci Eng A* 2020;795:140042.
- [43] Savage MF, Tatalovich J, Zupan M, Hemker KJ, Mills MJ. Deformation mechanisms and microtensile behavior of single colony Ti-6242Si. *Mater Sci Eng A* 2001;319:398–403.
- [44] Zheng Z, Waheed S, Balint DS, Dunne FPE. Slip transfer across phase boundaries in dual phase titanium alloys and the effect on strain rate sensitivity. *Int J Plast* 2018;104:23–38.
- [45] Zhao Z, Chen J, Guo S, Tan H, Lin X, Huang WD. Influence of alpha/beta interface phase on the tensile properties of laser cladding deposited Ti-6Al-4V titanium alloy. *J Mater Sci Technol* 2017;33:675–81.
- [46] Suri S, Viswanathan GB, Neeraj T, Hou DH, Mills MJ. Room temperature deformation and mechanisms of slip transmission in oriented single-colony crystals of an α/β titanium alloy. *Acta Mater* 1999;47:1019–34.
- [47] Luo P, McDonald DT, Xu W, Palanisamy S, Dargusch MS, Xia K. A modified Hall-Petch relationship in ultrafine-grained titanium recycled from chips by equal channel angular pressing. *Scr Mater* 2012;66:785–8.
- [48] Song ZY, Sun QY, Xiao L, Liu L, Wang H, Chen W, Sun J, Ge P. The influence of prior cold deformation on precipitation of alpha phase and variation of hardness in Ti-10Mo-8V-1Fe-3.5Al during aging treatment. *J Mater Res* 2009;24:452–8.
- [49] Zhao GH, Liang XZ, Kim B, Rivera-Diaz-del-Castillo PEJ. Modelling strengthening mechanisms in beta-type Ti alloys. *Mater. Sci. Eng. A* 2019;756:156–60.
- [50] Cizek L, Kratochvil P, Smola B. Solid-solution hardening of copper crystals. *J Mater Sci* 1974;9:1517–20.
- [51] Li H, Cai Q, Li S, Xu H. Effects of Mo equivalent on the phase constituent, microstructure and compressive mechanical properties of Ti–Nb–Mo–Ta alloys prepared by powder metallurgy. *J Mater Res Technol* 2022;16:588–98.
- [52] Ye XX, Chen B, Shen JH, Umeda J, Kondoh K. Microstructure and strengthening mechanism of ultrastrong and ductile Ti-xSn alloy processed by powder metallurgy. *J Alloys Compd* 2017;709:381–93.
- [53] Dini G, Ueji R, Najafizadeh A, Monir-Vaghefi SM. Flow stress analysis of TWIP steel via the XRD measurement of dislocation density. *Mater Sci Eng A* 2010;527:2759–63.
- [54] Umeda J, Tanaka T, Teramae T, Kariya S, Fujita J, Nishikawa H, Shibutani Y, Shen J, Kondoh K. Microstructures analysis and quantitative strengthening evaluation of powder metallurgy Ti–Fe binary extruded alloys with ($\alpha+\beta$)-dual-phase. *Mater Sci Eng A* 2021;803:140708.